Low-temperature ferromagnetism in perovskite $SrIrO_3$ films

Rachna Chaurasia,[1] K. Asokan,[2] Kranti Kumar,[3] and A. K. Pramanik[1,*]
[1]*School of Physical Sciences, Jawaharlal Nehru University, New Delhi 110067, India*
[2]*Materials Science Division, Inter-University Accelerator Centre, New Delhi 110067, India*
[3]*UGC-DAE Consortium for Scientific Research, Indore 452001, India*

(Received 14 September 2020; revised 7 December 2020; accepted 3 February 2021; published 11 February 2021)

The $5d$-based $SrIrO_3$ represents a prototype example of nonmagnetic correlated metal which mainly originates from a combined effect of spin-orbit coupling, lattice dimensionality, and crystal structure. Therefore tuning of these parameters results in diverse physical properties in this material. Here, we study the structural, magnetic, and electrical transport behavior in epitaxial $SrIrO_3$ film ($\sim$40 nm) grown on $SrTiO_3$ substrate. As opposed to bulk material, the $SrIrO_3$ film exhibits a ferromagnetic ordering at low temperature below $\sim$20 K. The electrical transport data indicate an insulating behavior where the nature of charge transport follows Mott's variable-range-hopping model. A positive magnetoresistance is recorded at 2 K which has a correlation with the magnetic moment. We further observe a nonlinear Hall effect at low temperature ($<$20 K) which arises due to an anomalous component of the Hall effect. An anisotropic behavior of both magnetoresistance and the Hall effect has been evidenced at low temperature, which, coupled with the anomalous Hall effect, indicates the development of ferromagnetic ordering. We believe that an enhanced (local) structural distortion caused by lattice strain at low temperatures induces ferromagnetic ordering, thus showing that structural instability plays a vital role in tuning the physical properties in $SrIrO_3$.

DOI: 10.1103/PhysRevB.103.064418

I. INTRODUCTION

In recent times, lots of scientific interest has been placed on Ir-based transition-metal oxides [1–8]. Due to their $5d$ character, iridates exhibit strong spin-orbit coupling (SOC) and a relatively weak electron correlation (U) effect. The delicate balance among competing energies such as SOC, U, and the crystal field effect (CFE) gives exotic electronic and magnetic properties in these materials where many of the phases are topologically relevant. In the presence of strong SOC, the t_{2g} d orbitals split into low-lying $J_{\text{eff}} = 3/2$ and top-lying $J_{\text{eff}} = 1/2$ states. In the case of Ir^{4+} with a $5d^5$ electronic configuration, the $J_{\text{eff}} = 3/2$ state is fully filled, while $J_{\text{eff}} = 1/2$ remains half filled. The latter J_{eff} state being narrow, even a small U opens up a gap, thus giving a realization of a $J_{\text{eff}} = 1/2$ Mott-like insulating state [1,2].

The built-in structural dimensionality has, however, a dominant role in the magnetic and electronic properties of iridium oxide materials. For instance, in the Ruddlesden-Popper (RP) series $Sr_{n+1}Ir_nO_{3n+1}$ (which can be considered as $SrO/(SrIrO_3)_n$, where n layers of perovskite $SrIrO_3$ is separated by a magnetically and electronically inactive SrO layer), a transition from a paramagnetic (PM) and metallic state in perovskite $SrIrO_3$ ($n = \infty$) to a magnetic and insulating state has been observed in layered Sr_2IrO_4 ($n = 1$) and $Sr_3Ir_2O_7$ ($n = 2$) [5,9–11]. Among the iridium oxides, the perovskite $SrIrO_3$ draws particular interest as it is shown to lie on the verge of ferromagnetic (FM) instability and metal-insulator transition (MIT) [12]. In addition, the low-temperature electronic state in $SrIrO_3$ has been characterized with a non-Fermi-liquid behavior [13]. Therefore tuning of parameters, such as SOC, U, structural distortion, etc., by means of doping or lattice strain is likely to modify its ground-state electronic and magnetic properties significantly. In fact, a recent band structure calculation shows a line node near the Fermi surface which is inherent to the crystal structure of this material and predicts that $SrIrO_3$ can host topological phases upon tuning the SOC strength with suitable doping [14]. Furthermore, the emergence of an antiferromagnetic (AFM) and insulating state with the substitution of a nonmagnetic and isovalent element in $SrIr_{1-x}Sn_xO_3$ highlights the role of structural-distortion-driven tuning of its physical properties [15].

In this paper, we have studied the magnetic and electrical transport behavior in an epitaxial $SrIrO_3$ film ($\sim$40 nm) grown on $SrTiO_3$ substrate. Bulk $SrIrO_3$ adopts a hexagonal structure grown in ambient conditions, but a perovskite orthorhombic crystal structure can be realized if synthesized under high pressure [6,16]. However, an epitaxial film grown on a suitable substrate has the advantage that it can host an orthorhombic $SrIrO_3$. Moreover, substrate strain can be used as a tuning parameter to get modified magnetic and electronic behavior. There have been several studies of $SrIrO_3$ film with different substrates. An angle-resolved photoemission spectroscopy (ARPES) study on perovskite $SrIrO_3$ film reveals a narrow semimetallic band across the Fermi level which mainly originates due to the combined effect of SOC, dimensionality, and IrO_6 octahedral rotations [17]. The effects of substrate strain, film thickness, and substrate temperature

*akpramanik@mail.jnu.ac.in

on metal-insulator transition in perovskite $SrIrO_3$ film have been studied [18–21]. For $SrIrO_3$ multilayers, many exotic phenomena such as the topological Hall effect, the anomalous Hall effect, tuning of magnetic anisotropy, exchange bias, etc., have also been studied in heterostructures consisting of $SrIrO_3$ and FM oxides [22–25]. While most of the studies have focused on exotic transport and electronic properties, less attention has been paid to the evolution of magnetic behavior in $SrIrO_3$ films. Dimensionality-controlled magnetic and electronic properties have recently been studied in artificial $[(SrIrO_3)_m, (SrTiO_3)_n]$ (m, $n = 1, 2, 3, ...$) superlattices [26,27]. These studies show a low-temperature magnetic ordering in the $SrIrO_3$ layer with the transition temperature around 140 K for m, $n = 1$ which systematically decreases with increasing m and further show a close relation of resistivity to the magnetic transition. A recent theoretical calculation shows that the magnetic state in bulk perovskite $SrIrO_3$ is significantly modified with the tuning of SOC [12]. Therefore the lattice strain or the distortion of local IrO_6 octahedra in films is likely to play a vital role in determining its magnetic behavior. A prominent example of strain-induced ferromagnetism is $CaRuO_3$ film, where its bulk component has a similar orthorhombic structure showing similar nonmagnetic and non-Fermi-liquid behavior [28].

The present $SrIrO_3$ film is found to be epitaxial with good crystal quality. While the magnetic data indicate a development of (weak) FM ordering at low temperature ($\lesssim$20 K), the film remains insulating over the entire temperature range. A positive, though small magnetoresistance (MR) is observed at 2 K which has a correlation with its magnetic behavior. The nonlinear Hall effect coupled with the anisotropic-MR and anisotropic-Hall effect further supports an evolution of the FM state at low temperature. An increasing strain or local structural distortion at low temperature is believed to induce the FM behavior.

II. EXPERIMENTAL METHODS

An epitaxial thin film of $SrIrO_3$ with thickness of ~40 nm has been grown on (100)-oriented $SrTiO_3$ single-crystal substrate using the pulsed laser deposition (PLD) technique equipped with a KrF ($\lambda = 248$ nm) laser. A phase-pure stoichiometric $SrIrO_3$ polycrystalline pellet is used as a target for film deposition. Before deposition, the substrate has been properly cleaned in ultrasonic cleaner alternatively with acetone and isopropyl alcohol for about 10 min. The laser frequency and energy used are 5 Hz and 1.5 J/cm^2, respectively. The deposition has been done with parameters such as a substrate-to-target distance of 5 cm, a substrate temperature of 750 °C, and an oxygen pressure during deposition of 0.1 mbar. In order to maintain the oxygen stoichiometry, the deposited films have been postannealed at the same deposition temperature, 750 °C, for about 15 min at a partial oxygen pressure around 500 mbar. The thickness of the films has been estimated using calibrated laser shot counts [29] and closely matches with the thickness checked with field emission scanning electron microscopy (FESEM). The structural characterization of the films is performed with x-ray diffraction (XRD), where the data have been collected using a PANalytical diffractometer equipped with a Cu-K_α source.

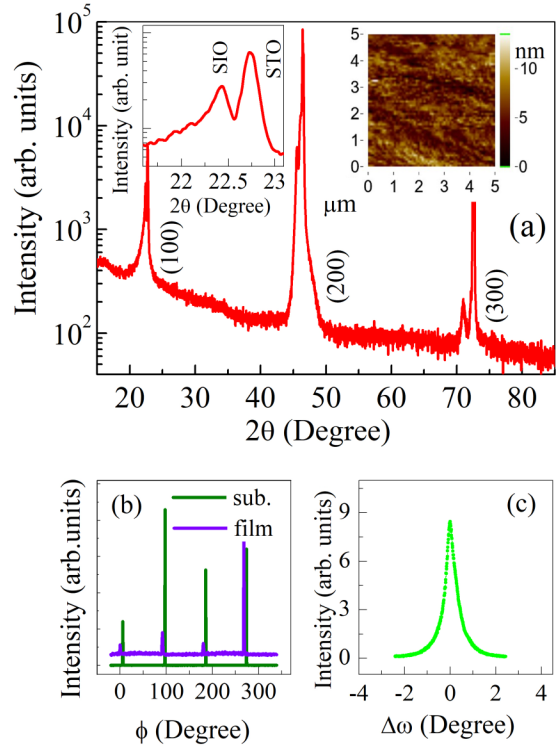

FIG. 1. (a) The XRD pattern of $SrIrO_3$ film grown on $SrTiO_3$ (100) substrate is shown in semilog scale. The left inset shows the expanded (100) Bragg peak with thickness fringes, while the right inset presents an atomic force microscope image of the film showing surface topography. (b) The ϕ scan at (220) reflection. (c) The ω scan (rocking curve) of the $SrIrO_3$ film around (200) reflection. SIO, $SrIrO_3$, STO, $SrTiO_3$, sub., substrate.

X-ray absorption spectroscopy (XAS) data have been collected from the National Synchrotron Radiation Research Center, Taiwan, for the O K edge and Ir L_3 edge in total electron yield and fluorescence modes, respectively, following standard procedure. Before XAS measurements, the x-ray photon energy has been calibrated using a metallic gold foil for L_3 edge absorption, which is the standard procedure followed in the beamline. Furthermore, XAS data are collected for various iridate samples having different Ir charge states in the same beamtime and same beamline, which provides a better comparison. The electronic transport and its angle-dependent measurements are done using a four-probe method in an insert attached with a 9-T magnet (NanoMagnetics Instruments). Both temperature- and magnetic-field-dependent magnetic properties of the film are measured with a superconducting quantum interference device (Quantum Design). The magnetic contribution due to the film has been extracted after subtracting the related moment of the substrate.

III. RESULTS AND DISCUSSION

A. Structural analysis with x-ray diffraction

Figure 1(a) shows a θ-2θ x-ray diffraction (XRD) plot of $SrIrO_3$ film deposited on $SrTiO_3$ (100) substrate. Bulk $SrIrO_3$ is realized from the Ruddlesden-Popper series $Sr_{n+1}Ir_nO_{3n+1}$ with $n = \infty$, where infinite layers of perovskite $SrIrO_3$ are

stacked together forming a three-dimensional structural network. Bulk $SrIrO_3$ generally adopts two different crystal structures based on the synthesis protocol. At ambient pressure, $SrIrO_3$ crystallizes in a 6*H*-hexagonal (monoclinic) structure, while using a high-pressure synthesis method, this material stabilizes in a perovskite orthorhombic (*Pbnm*) structure. As a target material for deposition of the present film, single-phase $SrIrO_3$ is used which has been synthesized at ambient pressure having monoclinic-$C2/c$ structure with lattice parameters $a = 5.5982$ Å, $b = 9.6293$ Å, $c = 14.1949$ Å, and $\beta = 93.228^\circ$. The epitaxial growth of films has, however, the advantage that a metastable orthorhombic phase can be stabilized with perovskite substrate. The substrate used, $SrTiO_3$, has cubic structure with lattice parameter $a_{\text{sub}} = 3.90$ Å. The pseudocubic (pc) lattice parameter a_{pc} ($\approx 0.5\sqrt{a^2 + b^2}$) of the target $SrIrO_3$ has been calculated from its bulk orthorhombic lattice parameters ($a = 5.56$ Å, $b = 5.59$ Å, and $c = 7.88$ Å), giving a value of 3.942 Å, which corresponds to approximately +1% compressive lattice strain for the films deposited on $SrTiO_3$. Given that a_{pc} and a_{sub} have a slight mismatch, while the lattice parameter c of orthorhombic $SrIrO_3$ matches closely with $2a_{\text{sub}}$, the $SrIrO_3$ films on $SrTiO_3$ (100) substrate are likely to grow along the (110) direction rather than having (100) orientation.

As shown in Fig. 1(a), the XRD pattern of deposited film exhibits only crystalline peaks without a trace of any impurity or additional phase(s). A satellite peak near the substrate peak signifies the epitaxial growth of the $SrIrO_3$ film. A magnified view of the low-angle (100) reflection is shown in the left inset of Fig. 1(a) with thickness fringes. While the peaks due to substrate and film are not superimposed, they are very close, which implies that the film is under strain. The Bragg peaks related to $SrTiO_3$ and $SrIrO_3$ are observed at $2\theta = 22.74^\circ$ and $\theta = 22.44^\circ$, which gives the lattice parameter values of 3.90 and 3.96 Å, respectively. The calculated lattice parameter of the $SrIrO_3$ film is very close to its bulk a_{pc} (3.942 Å). The $SrTiO_3$ substrate in reality gives a compressive strain of approximately +1.5% to $SrIrO_3$ film.

Furthermore, an estimation regarding the thickness D of deposited film has been done using thickness fringes in (100) reflection with the following formula:

$$D = \frac{(m-n)\lambda}{2(\sin\theta_m - \sin\theta_n)}, \tag{1}$$

where θ_m and θ_n are the positions of the mth and nth order peaks and λ is the wavelength of x ray used. Following Eq. (1), we have calculated the thickness of the $SrIrO_3$ film to be ∼39.7 nm, which is close to the expected value (∼40 nm) from growth rate estimation.

An AFM image of the film surface is shown in the right inset of Fig. 1(a). The AFM image shows no voids but an average surface roughness of ∼1 nm. To further understand the structure of the deposited film, a ϕ scan has been taken at (220) reflection for both film and $SrTiO_3$ substrate, as shown in Fig. 1(b). The $SrTiO_3$ has fourfold symmetric cubic structure with an in-plane and out-of-plane pseudocubic lattice parameter of 3.90 Å. As seen in Fig. 1(b), the $SrTiO_3$ and $SrIrO_3$ ϕ-scan peaks are nearly equidistant, ∼90° apart, and the peaks are close to each other, having a very small difference with $\Delta\phi \sim 5.5^\circ$. This suggests that there is a fourfold structural symmetry of the $SrIrO_3$ film and that the film has a single domain with cube-on-cube growth. Moreover, an unsplit nature of peaks in the ϕ-scan data [Fig. 1(b)] is in favor an orthorhombic structure rather than a monoclinic one [21]. The θ-2θ XRD pattern and the ϕ scan underline the fact that the present $SrIrO_3$ film has taken an orthorhombic structure on $SrTiO_3$ substrate. Our result is in line with previous reports which have shown that a film thinner than 40 nm would take an orthorhombic structure while a thicker film is susceptible to a mixed phase of monoclinic and orthorhombic structures [30,31]. We have further characterized the crystalline quality of the deposited $SrIrO_3$ film with a ω scan (rocking curve) in XRD measurements. Figure 1(c) shows the ω scan of the present $SrIrO_3$ film, obtained around (200) reflection. The full width at half maximum (FWHM) of the ω scan has been calculated to be around 0.5°, which compares well with other reports of similarly thick films [20,21]. The ω scan usually signifies the perfection in lattice planes and mosaic spread; therefore a reasonably small FWHM suggests that the present film has parallel planes and less mosaic spread. All these results conclusively show that the present $SrIrO_3$ film is a high-quality epitaxial film with an orthorhombic structure, obtained on $SrTiO_3$ substrate.

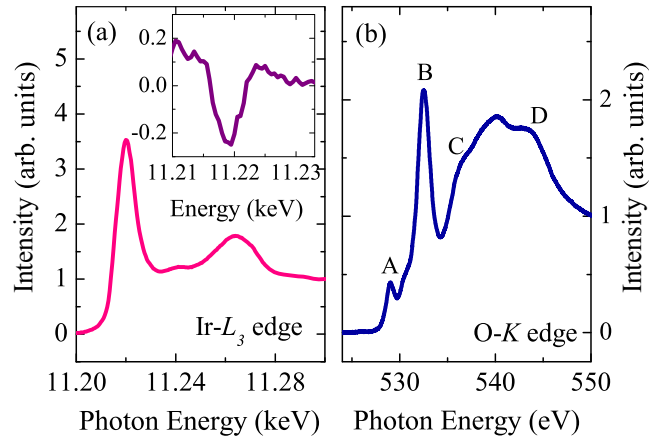

FIG. 2. (a) XAS spectra at the Ir L_3 edge and (b) XAS spectra at the O K edge of the $SrIrO_3$ film are shown at room temperature. The inset of (a) shows the double derivative of XAS spectra of the Ir L_3 edge. A, B, C, and D in (b) mark the energy position for the peak or hump.

B. X-ray absorption spectroscopy

To understand the Ir oxidation state as well as Ir-O hybridization in the present film, x-ray absorption spectroscopy (XAS) measurements have been done at room temperature. Figure 2(a) shows normalized L_3 ($2p_{3/2} \rightarrow 5d$) absorption edge spectra for the $SrIrO_3$ film which involves transition to both $5d_{5/2}$ and $5d_{3/2}$ states. It is evident in Fig. 2(a) that the L_3 edge occurs at 11 219.5 eV. Usually, in XAS spectra the position of the absorption edge largely depends on the ionic state of the transition metal because the transition-metal–oxygen bond length mostly determines the energy shifting of the absorption edge. With an increase in ionic state the bond length becomes shortened; therefore the energy edge occurs at higher energy. However, a small difference in edge

position has been observed even for the same ionic state with different lattice structure. In the case of thin films where the lattice strain has a significant role in the bond length, the position of the absorption edge may vary with the bulk material. In the case of iridium, the Ir L_3 absorption edge has usually been seen to occur at 11 218.0, 11 219.6, 11 220.0, 11 222.0, and 11 222.5 eV for the Ir, Ir^{3+}, Ir^{4+}, Ir^{5+}, and Ir^{6+} charge states, respectively [32–37]. Given that the absorption edge is very sensitive to the local environment of anions, a small difference in energy position may occur from system to system. The L_3 edge at 11 219.95(4) eV in the present film suggests that iridium is in the Ir^{4+} state. However, a little lower value of edge position compared with 11 220 eV may be due to the strain effect in film giving a modified Ir–O bond length or due to the presence of a small fraction of Ir^{3+} related to oxygen vacancy during film deposition. While there is a difference in peak position even for the same element in different materials which is mainly due to different chemical environments and compositions [32,35,36], the fact is that the absorption edge increases with increasing charge state. In this sense, the L_3 XAS data imply a Ir^{4+} charge state in the present film. To check whether there is any mixing of Ir oxidation states, we have plotted the double derivative in the inset of Fig. 2(a). A distinct shoulder in the double derivative of the L_3 spectra is generally considered to be indicative of a mixed charge state [32], but no clearly visible shoulder in the double derivative of our L_3 spectra is observed, as shown in the inset of Fig. 2(a). Thus, based on these results, we conclude that iridium mostly is in the Ir^{4+} oxidation state.

We have additionally measured XAS spectra at the O K edge on the present film to understand about hybridization between Ir $5d$ and O $2p$ states. Following crystal field chemistry, the Ir d orbitals in the environment of IrO_6 octahedra are split into low-lying t_{2g} (d_{xy}, d_{yz}, and d_{zx}) and high-lying e_g ($d_{x^2-y^2}$ and d_{z^2}) states. In the octahedral environment, the oxygen orbitals (p_x, p_y, and p_z) of six ligands (four basal and two apical) hybridize with transition-metal d orbitals. Among t_{2g} orbitals, d_{xy} hybridizes only with basal p_x/p_y, while d_{yz} and d_{zx} hybridize with both basal p_z and apical p_x/p_y orbitals. In the case of e_g orbitals, $d_{x^2-y^2}$ and d_{z^2} engage in interaction with p_x/p_y and p_z, respectively. The normalized O K edge spectra for the present film in Fig. 2(b) show two distinct peaks (marked as A and B in the plot) in the lower-energy regime at binding energy E_b around 529 and 532.5 eV, respectively, while a broad hump is observed between 534 and 550 eV. The onset energy of the present O K spectral edge agrees with another report for $SrIrO_3$ film [34]. The peak at 529 eV (marked as A) is due to hybridization between Ir d_{xz}/d_{yz} and apical O p_x/p_y, while that at 532.5 eV (marked B) arises due to interaction between Ir t_{2g} and basal O p orbitals. On the other hand, the hybridization between the Ir e_g and O p orbitals causes the broad hump on the higher-energy side. It can be further noticed in Fig. 2 that the broad hump on the high-energy side exhibits two prominent shoulders [marked as C and D in Fig. 2(b)]. While the above hybridization picture has been discussed considering an isolated model of e_g and t_{2g} orbitals, a recent theoretical study has, however, shown that in $5d$-based oxides, the crystal field effect, SOC, and U have a prominent role in the mixing of e_g and t_{2g} orbitals and hence influence the absorption edge spectra [38]. Furthermore, note that we observe a slight difference in peak positions compared with bulk materials, which is probably due to substrate-induced strain in films, which alters the extent of hybridization through local structural modification. Such modification in strength of hybridization *vis-à-vis* peak position in XAS O K edge spectra has been observed with chemical pressure in $(Y_{1-x}Pr_x)_2Ir_2O_7$ [35].

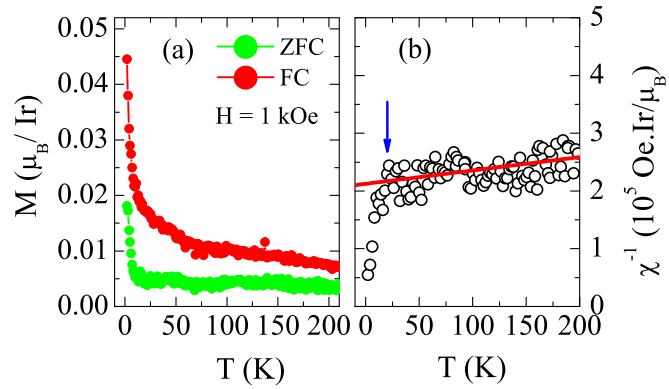

FIG. 3. (a) Temperature-dependent magnetization data measured in a 1-kOe applied field following ZFC and FC protocols are shown for $SrIrO_3$ film. (b) The inverse magnetic susceptibility χ^{-1} [$= (M/H)^{-1}$] as a function of temperature, deduced from ZFC magnetization data. The red straight line is due to fitting of the straight line following the Curie-Weiss law (discussed in text), while the arrow indicates the deviation from linearity.

C. Magnetization study

Figure 3(a) shows the temperature-dependent magnetization M data for $SrIrO_3$ film, collected in an applied field of 1 kOe following zero-field cooling (ZFC) and field cooling (FC) protocols. The moment of the film has been extracted after subtracting the substrate contribution. On cooling, while the ZFC and FC branches of magnetization exhibit a finite difference starting from high temperature, the moment in both measurements increases monotonically till about 20 K. Below 20 K, both M_{FC} and M_{ZFC} show a sharp increase till the lowest measurement temperature of 2 K. This sharp increase in moment below ~20 K implies a development of weak ferromagnetism in $SrIrO_3$ film at low temperature. However, the moment of the film is quite low, which is in line with the fact that iridates are generally low-moment systems. Note that both the low-temperature FM state and the obtained moment are in agreement with artificial $[(SrIrO_3)_m, (SrTiO_3)_n]$ superlattices [26,27]. Furthermore, the observed magnetic behavior of $SrIrO_3$ film is consistent with our recent report of exchange bias behavior in $La_{0.67}Sr_{0.33}MnO_3/SrIrO_3$ multilayers at low temperature below ~20 K [24]. Note that a similar sharp rise in susceptibility has also been observed in bulk $SrIrO_3$ below ~15 K which has been shown to be due to proximity to FM instability [13]. At low temperatures, there is significant exchange enhancement, though a FM ordering, which probably requires a triggering, is not developed. In fact, similar ferromagnetic instability has been predicted in theoretical calculations for bulk $SrIrO_3$ [12]; hence any suitable

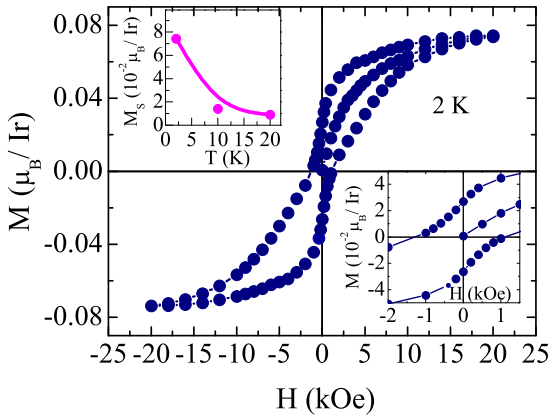

FIG. 4. Magnetic-field-dependent magnetization loop is shown for $SrIrO_3$ thin film at 2 K. The upper inset shows the variation of saturated magnetization M_s with temperature. The lower inset depicts an expanded view of $M(H)$ close to the origin showing an asymmetry in the magnetic hysteresis loop.

perturbation is likely to trigger the magnetism in this material. Along with chemical doping [15,39], the lattice strain arising from the underlying substrate acts as a driving force to induce a magnetic state in films. Furthermore, the inverse magnetic susceptibility χ^{-1}, calculated as $(M_{ZFC}/H)^{-1}$, is shown in Fig. 3(b) as a function of temperature. As evident in Fig. 3(b), above 20 K, $\chi^{-1}(T)$ shows a linear increase where the behavior is similar to Curie-Weiss (CW) behavior, $\chi = C/(T - \theta_P)$, where C and θ_P are the Curie constant and Curie temperature, respectively. However, fitting parameters such as C and θ_P cannot be determined precisely. Nonetheless, the deviation from linear behavior of $\chi^{-1}(T)$ below around 20 K suggests an onset of FM at low temperature.

To understand the low-temperature magnetic state further, we have recorded the magnetic hysteresis loop $M(H)$ at three different temperatures, 2, 10, and 20 K, with a field range of ±20 kOe. The magnetic contribution due to the $SrTiO_3$ substrate has been subtracted from the original $M(H)$ data at each temperature. We have adopted the protocol where a slope in the $M(H)$ data has been taken at the high-field regime. Assuming this slope represents the susceptibility of the substrate, the moment of the substrate has been calculated, which has been used for subtraction to obtain the moment of the film. Figure 4 shows the representative corrected $M(H)$ plot for the present $SrIrO_3$ film at 2 K. Unlike bulk $SrIrO_3$, the $M(H)$ plot shows an open hysteresis, where we find left and right coercive fields $H_c^L = 1293$ Oe and $H_c^R = 1109$ Oe and upper and lower remnant magnetizations $M_r^U = 2.69 \times 10^{-2}$ μ_B/Ir and $M_r^L = 2.63 \times 10^{-2}$ μ_B/Ir, respectively. This asymmetry in the $M(H)$ plot ($H_c^L \neq H_c^R$), which is clearly shown in lower inset of Fig. 4, generally arises due to an exchange bias (EB) effect. For the present film, we calculate an exchange bias field H_{EB} [$= (|H_c^L + H_c^R|)/2$] around 92 Oe at 2 K which reduces to about 81 Oe at 10 K. Usually, the EB effect is realized when a system with an FM-AFM interface is cooled in the presence of a magnetic field from high temperature and $M(H)$ is measured at low temperature [40]. The applied field biases the exchange interaction at the interface, which results in a shifting of the $M(H)$ plot or EB phenomena [24,29,41]. However, the interfaces in films or multilayers experience various other factors, such as structural distortion, electronic reconstruction, strain, etc., which modify the magnetic character at the interface accordingly [42,43]. These in turn induce the EB effect which has shown many, many interesting properties. For instance, the EB effect has been observed even in zero-field-cooled $M(H)$ plots [24,29] and in single-layer magnetic films [44], which is rather unusual. The observed EB effect in the present single-layer $SrIrO_3$, deposited on diamagnetic $SrTiO_3$, is likely due to the strain effect. We speculate that due to an enhanced strain at the interface, some $SrIrO_3$ layers adjacent to the interface may achieve an antiferromagnetic ordering which in contact with the rest of the ferromagnetic $SrIrO_3$ layers results in an exchange bias effect.

Figure 4 further shows a saturation in moment within an applied field of 20 kOe. The temperature variation of the saturation moment M_s is shown in the upper inset of Fig. 4. We have obtained a very low M_s which, however, agrees well with other studies of $[(SrIrO_3)_m, (SrTiO_3)_n]$ superlattices [26,27]. While iridates generally exhibit a low moment, the obtained M_s is much lower than the expected saturation moment of 0.33 μ_B/Ir, which can be calculated using $M_s = g_J J_{\text{eff}} \mu_B$ with $g_J = 2/3$ and $J_{\text{eff}} = 1/2$ for strong-SOC-dominated systems. For instance, at 2 K we obtain a saturation moment around 7.5×10^{-2} μ_B/Ir (upper inset in Fig. 4) which is roughly one order lower than the expected value following the J_{eff} model. A detailed investigation involving the microscopic tools is required to understand the nature of low-temperature magnetism in the present film. However, at this stage we can speculate that the nature of this low-temperature magnetic state may be either of FM type without the J_{eff} state or a canted-AFM type with a J_{eff} state. It can be noted that a weak FM has been observed in layered iridate Sr_2IrO_4 due to canted-AFM ordering which is driven by Dzyaloshinskii-Moriya (DM) type antisymmetric interaction in this SOC-dominated system [1,2]. While the rest of the results and analysis suggests a FM ordering at low temperature in the present film (discussed later), with the progress of time the J_{eff} model has been shown to deviate considerably in a nonideal (or distorted) octahedral arrangement in both theoretical and experimental studies. A recent theoretical study has even discussed the CFE, SOC effect, and U effect on the mixing of e_g and t_{2g} states in $5d$ oxides [38]. Very recently, an evolution of both spin and orbital moment has been shown with the lattice distortion in the $3d$-$5d$ double perovskite $(Sr_{1-x}Ca_x)_2FeIrO_6$ [45]. Therefore the magnetism in iridates continues to be an interesting subject of research.

Nonetheless, the combination of EB effect, open hysteresis loop in $M(H)$ plot, and the magnetic saturation in $M(H)$ above 10 kOe imply the ferromagnetic nature of the present $SrIrO_3$ film at low temperature. The thermal demagnetization of the saturation moment, as shown in the upper inset of Fig. 4, further indicates low-temperature ferromagnetic ordering in the $SrIrO_3$ film. As opposed to the paramagnetic bulk $SrIrO_3$, this development of ferromagnetism in its films is quite noteworthy. We believe that epitaxial lattice strain in films plays an important role in stabilizing the FM state, which has been similarly observed in another nonmagnetic perovskite material, $CaRuO_3$ [28].

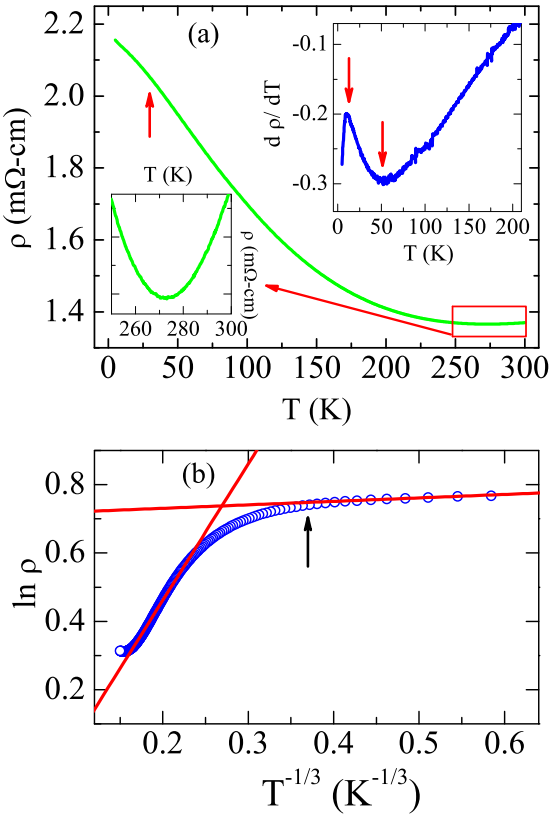

FIG. 5. (a) The electrical resistivity as a function of temperature is shown for $SrIrO_3$ film deposited on a $SrTiO_3$ substrate. The up arrow marks an anomaly in resistivity around its magnetic transition. The upper inset shows the temperature derivative of the resistivity data, showing the anomaly at low temperature as indicated by down arrows. The lower inset shows a magnified view of the metal-to-insulator transition around 272 K. (b) The fitting of data with the Mott variable-range-hopping model [Eq. (2)] in two different temperature ranges. The solid lines are due to straight line fittings with Eq. (2). The arrow indicates the deviation from linearity in fitting at low temperature around 20 K.

D. Temperature-dependent electronic transport measurements

To understand the electronic transport behavior in the present $SrIrO_3$ film, we have measured the temperature-dependent resistivity $\rho(T)$, as shown in Fig. 5. The resistivity value at room temperature is found to be ∼1.5 mΩ cm, which is in good agreement with earlier reports (1–2 mΩ cm) [18]. With decreasing temperature, the $\rho(T)$ increases monotonically indicating a semimetallic or insulating behavior. The electronic transport behavior in $SrIrO_3$ films is shown to be extremely sensitive to the deposition temperature, film thickness, and lattice strain [18–21]. Previous studies with varying substrate temperature (500–800 °C) have shown that with increasing substrate temperature, the film resistivity increases leading to an insulating behavior which is mainly due to an inhomogeneous Ir distribution [19]. Furthermore, epitaxial strain realized from either reducing film thickness or using lattice mismatch substrates has a prominent role in increasing the resistivity as well as in inducing the insulating state. Given that our substrate deposition temperature is 750 °C and the substrate $SrTiO_3$ has some lattice mismatch with $SrIrO_3$, this semimetallic or insulating behavior is a likely behavior. However, an overall low resistivity and a reasonably low ρ(5 K)-to-ρ(300 K) ratio (∼1.4) suggest a metal-like transport as for its bulk counterpart.

Moreover, a close inspection reveals a dip in the $\rho(T)$ data around 272 K, which has been shown in the lower inset of Fig. 5(a). This dip in $\rho(T)$ appears to be a metal-insulator transition (MIT) which has been similarly observed at different temperatures in $SrIrO_3$ film with different substrates as well as with different film thicknesses [18,20,21]. Here, it can be noted that below this dip, the $\rho(T)$ does not follow any logarithmic temperature dependence, which is typical of the Kondo phenomenon. On cooling, a change in slope in $\rho(T)$ is further evident at low temperature around 30 K, which is marked by an up arrow in Fig. 5(a). This change in slope in $\rho(T)$ occurs around its magnetic transition, which is prominently observed in its temperature derivative, $d\rho/dT$, where a maximum slope change is observed around 50 and 10 K (marked by down arrows), as shown in the upper inset of Fig. 5(a). The dip and peak in $d\rho/dT$ around 50 and 10 K, respectively, suggest that the resistivity changes with a relatively faster rate between these temperatures. However, there is a disagreement between the dip temperature in $d\rho/dT$ around 50 K and the magnetic ordering temperature in Fig. 3 which may be due to an early onset of magnetic ordering. Nonetheless, the anomaly in $\rho(T)$ at low temperature is connected with the magnetic ordering which has been similarly observed in $[(SrIrO_3)_m, (SrTiO_3)_n]$ $(m, n = 1, 2, 3, ...)$ superlattices [26,27].

The $\rho(T)$ data can be fitted using Mott's variable-range-hopping (VRH) model [46],

$$\rho = \rho_0 \exp[(T_0/T)^{\alpha}], \tag{2}$$

$$T_0 = \frac{21.2}{k_B N(\epsilon_F)\xi^3}, \tag{3}$$

where α is related to the dimensionality d of the system with $\alpha = 1/(d+1)$, T_0 is the characteristic temperature related to the leakage rate of localized states at the Fermi level, k_B is the Boltzmann constant, $N(\epsilon_F)$ is the density of states (DOS) at the Fermi level, and ξ is the localization length [47]. As shown in Fig. 5(b), Eq. (2) can be fitted with $\rho(T)$ in two distinct temperature regimes (5–15 K and 67–205 K) with $d = 2$, giving T_0 values of 3.7×10^{-4} K and 22.56 K, respectively. T_0 exhibits distinctly low values in the low-temperature magnetic state. T_0 is inversely proportional to both $N(\epsilon_F)$ and ξ [Eq. (3)]. Given that this is an insulating system, an increase in $N(\epsilon_F)$ at low temperature is very unlikely. Therefore this change in T_0 can be explained with an increase in ξ, suggesting that the localization length increases drastically with an onset of magnetism at low temperature.

E. Magnetoresistance

To further understand electron transport behavior, we have measured isothermal sheet resistance as a function of magnetic field (up to 85 kOe) at 2 K, where the field has been applied parallel to the plane of the film ($H \parallel ab$ plane). The resistance R has been measured with field applied in both

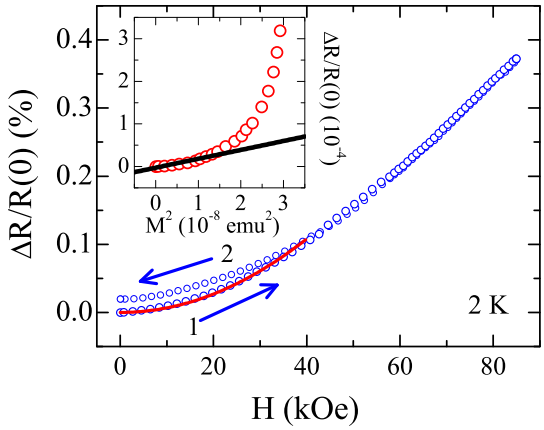

FIG. 6. Magnetoresistance (defined in text) as a function of magnetic field is shown for $SrIrO_3$ film at 2 K with only positive field direction. The arrows indicate the direction of field application. The solid line is due to fitting of MR data with quadratic field dependence. The inset shows the quadratic dependence of magnetoresistance on magnetization.

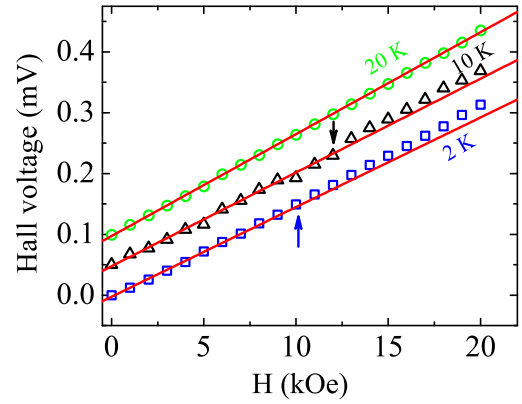

FIG. 7. Hall voltage vs magnetic field is shown at three different temperatures, i.e., 2, 10, and 20 K. The data at 10 and 20 K are vertically shifted by 0.1 and 0.2 mV, respectively, for clarity. The vertical arrows indicate the deviation from linearity at respective fields.

positive and negative directions. The percentage magnetoresistance (MR), $\Delta R/R(0) = [R(H) - R(0)]/R(0) \times 100$, has been calculated from measured resistance for the present $SrIrO_3$ film at 2 K and is shown in Fig. 6 with positive field direction. The film shows positive MR, i.e., resistance increases with applied magnetic field. The calculated value of MR is ∼0.33% at 80 kOe, which is not significant but agrees with other reports [20]. We, however, do not observe any cusp or peak in MR close to zero field, which is usually seen due to the weak antilocalization effect in strong-SOC systems. Interestingly, a hysteresis in the MR data between increasing and decreasing field has been observed below around 40-kOe field. This hysteresis in MR appears to be connected with the magnetic state of film at low temperature, as similarly a remnant magnetization has been observed in the $M(H)$ plot (Fig. 4). With application of a high magnetic field, there is an induced FM moment which is retained even after the applied field returns to zero. Given that FM spin ordering has a significant effect on charge transport behavior (Fig. 5), the difference in moment between increasing and decreasing field causes hysteresis in MR. In the high-field regime (>40 kOe), hysteresis is not evident due to magnetic saturation. To check further, we have plotted MR as a function of M^2 in the inset of Fig. 6. The MR follows a linear behavior with the square of magnetization in the field range up to ∼5 kOe, and after that the increase in moment does not scale with that of MR. This is clear in Fig. 4, which shows a faster increase in moment up to ∼5 kOe, and after that the rate of increase in moment slows down. In the low-field regime (below ∼40 kOe), the MR follows a quadratic field dependence, MR $\propto B^2$, as shown in Fig. 6 with a solid line.

F. Hall measurements

With the aim of investigating the nature of charge carriers and the magnetic state, the Hall voltage has been measured as a function of the magnetic field in the low-temperature magnetic state at 2, 10, and 20 K with $H \parallel ab$ plane. Figure 7 shows that the Hall voltage is linear with field (up to 20 kOe) at 20 K but with a lowering in temperature a nonlinearity is introduced where the onset field for nonlinearity decreases with decreasing temperature. Here, it can be noted that the FM state in the present film dominates or $M(T)$ shows a steep rise below around 20 K (Fig. 3). A nonlinear Hall effect is an intrinsic phenomenon which can be explained with various theoretical descriptions, where the two-carrier transport model and anomalous Hall effect (AHE) are commonly noted ones. Considering that the film develops a FM ordering at low temperature (Fig. 3) and MR follows a quadratic field dependence signifying a single carrier charge transport (Fig. 6), we have focused on AHE to understand the present Hall effect behavior. In general, Hall resistivity ρ_{xy} can be expressed as

$$\rho_{xy} = R_0 H + 4\pi R_s M, \tag{4}$$

where H is the magnetic field and M is magnetization. While the first term is due to Lorentz-force-driven ordinary Hall resistivity, the second term represents the contribution from the anomalous Hall effect. The AHE typically arises in FM materials with broken time-reversal symmetry. While the ordinary Hall effect is due to the Lorentz force effect, the origin of the anomalous part is debated. Though the mechanisms based on intrinsic or extrinsic (skew scattering and side jump) scattering are usually thought to cause the anomalous Hall effect, the SOC effect plays a crucial role in all these mechanisms [48]. As seen in Eq. (4), the AHE is proportional to magnetization and can effectively be used to investigate the magnetic state of a material. Following Eq. (4), in Fig. 8(a) we have plotted the Hall coefficient R_H $(=\rho_{xy}/H)$ as a function of magnetic susceptibility $(=M/H)$ at 2 K. A good linear fit to the experimental data is obtained in the high-field regime, as shown in Fig. 8(a). From fitting, we obtain $R_0 = -2.5881$ cm^3/C and $R_s = 4.35 \times 10^3$ cm^3/C at 2 K. R_s, which is related to the magnetic part, is roughly three orders higher than R_0 as observed in ordinary magnetic materials. The negative sign of R_0 implies electronlike charge carriers in the system. The variation of both R_0 and R_s at low temperatures is shown in the inset of Fig. 8(a), showing that both the parameters

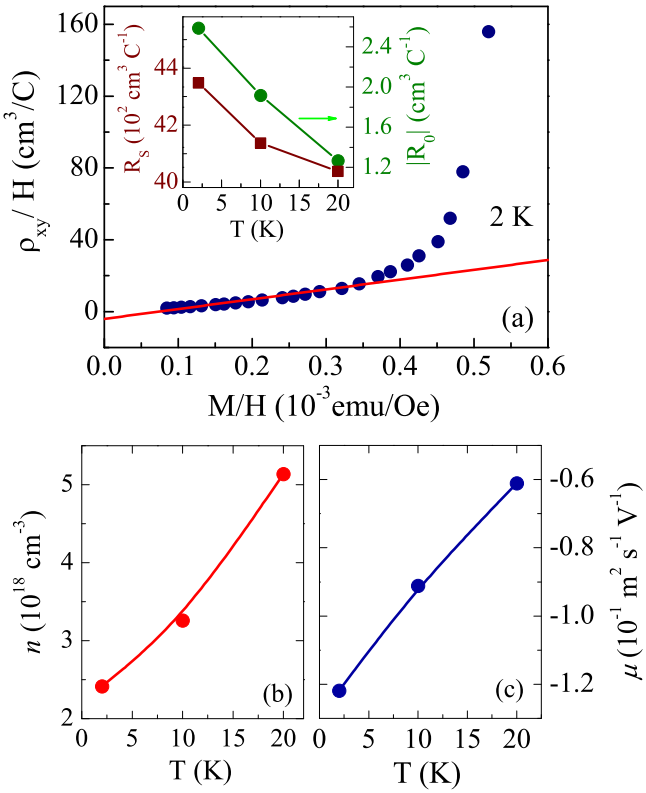

FIG. 8. (a) Hall coefficient R_H $(=\rho_{xy}/H)$ vs magnetic susceptibility $(=M/H)$ is shown at 2 K following Eq. (4) for $SrIrO_3$ film grown on $SrTiO_3$. The inset shows the calculated values of $|R_0|$ and R_s with temperature. (b) and (c) The variation of carrier concentration n and carrier mobility μ, respectively, at low temperatures.

increase with the lowering of the temperature. From the relation $R_0 = -1/(ne)$, we obtain carrier concentration $n = 2.4 \times 10^{18}/\text{cm}^3$ at 2 K, which is in good agreement with earlier reports and indicates low carrier concentration in the system [18]. The mobility of charge carriers has also been evaluated as $\mu = R_0/\rho_{xx}$, where ρ_{xx} is the resistivity parallel to the direction of current in the presence of zero magnetic field. Calculated values of n and μ for different temperatures are shown in Figs. 8(b) and 8(c), respectively. Both charge concentration and mobility decrease with decreasing temperature. Nonetheless, the presence of the nonlinear Hall effect or anomalous Hall effect confirms a development of FM ordering at low temperature below ~20 K in the present film. This is in contrast to bulk $SrIrO_3$, which exhibits PM behavior at least down to 1.7 K, though a sharp rise in susceptibility below 15 K indicates that this material is in proximity to FM instability [13].

G. Angle-dependent Hall and resistivity measurements

The low-temperature FM state has further been probed by measuring both longitudinal (R_{xx}) and transverse (R_{xy}) resistance after rotating the film with respect to the direction of the applied magnetic field. In the case of FM materials with long-range spin ordering, the magnetization has an influence on the scattering of carriers, and the resistivity depends on the angle between magnetization (or magnetic field) and current

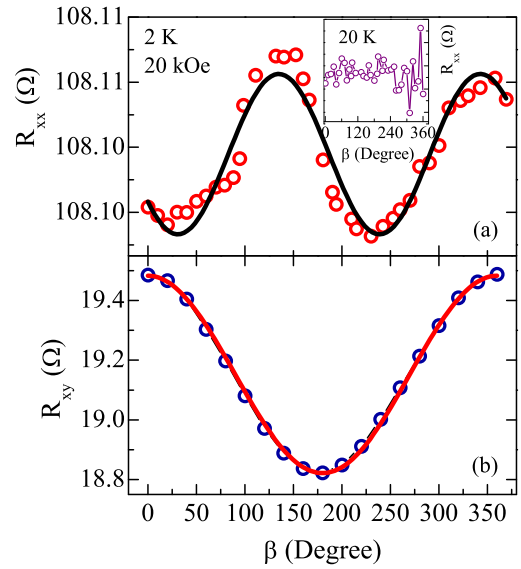

FIG. 9. Angular dependence of (a) longitudinal resistance R_{xx} and (b) transverse resistance (planar Hall) is shown for the present $SrIrO_3$ film at 2 K with an applied field of 20 kOe. The inset of (a) shows the angular dependence of R_{xx} at 20 K with a 20-kOe field.

directions, which is usually termed anisotropic magnetoresistance (AMR) and defined as the difference in MR when the current I is applied either parallel or perpendicular to the magnetization. Figures 9(a) and 9(b) show the measured R_{xx} and R_{xy} as a function of angle β between the magnetization and the current direction, respectively. The measurements have been done at 2 K in the presence of a 20-kOe field, where the applied field is in the range of saturation magnetization (see Fig. 4). Though the variation of R_{xx} over angle β is not significant, it shows a sinusoidal variation where the $R_{xx}(\beta)$ data are best fitted with the following equation:

$$R_{xx} = A + B\cos(C\beta + D), \tag{5}$$

where A is an offset parameter, B is the amplitude of the angular dependence of the MR, C is the multiplying factor to angle, and D is the phase factor. Usually, the parameter C takes a value of 2, but in the present case, $C = 1.75(3)$ gives a better fit with phase factor $D = 126(5)^\circ$. The variation of R_{xx} with angle β implies that the film develops FM ordering at low temperature. In the inset of Fig. 9(a), we have shown the same $R_{xx}(\beta)$ collected at 20 K. As seen in the figure, R_{xx} does not exhibit any noticeable angular dependence at 20 K, which is in agreement with the linear Hall effect evidenced at the same temperature (Fig. 7). This is primarily because at 20 K or above, the FM ordering is not strong enough to induce an angular dependence, or it requires a higher magnetic field. We have further recorded planar Hall resistance R_{xy} as a function of angle β in Hall geometry where current is applied in the xx direction and voltage is measured in the xy direction. As shown in Fig. 9(b), the variation of R_{xy} is also sinusoidal with β and can be best fitted using Eq. (4) with $C = 1$ and negligible phase factor D. Nonetheless, the dependence of both R_{xx} and R_{xy} on the angle (β) between the applied current and magnetic field direction supports a low-temperature FM ordering in the present film.

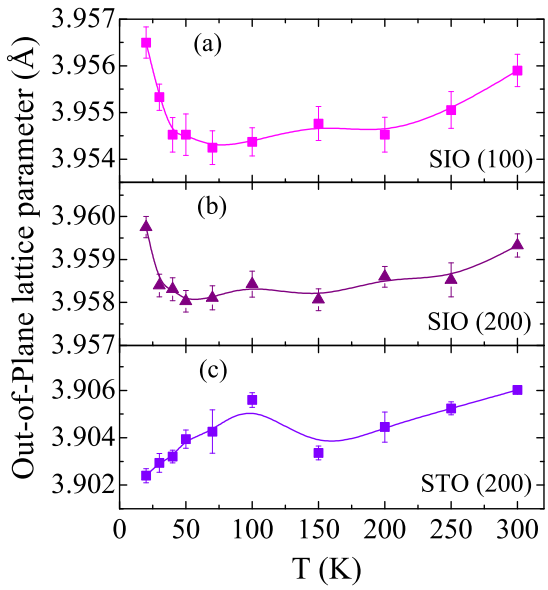

FIG. 10. (a) and (b) The lattice parameter of $SrIrO_3$ film calculated from (100) and (200) Bragg reflection, respectively. (c) The lattice parameter of $SrTiO_3$ substrate due to (200) Bragg reflection.

H. Temperature-dependent structural investigation

Our previous results indicate an unusual FM state in $SrIrO_3$ film at low temperature which we believe is caused by an enhanced strain or structural distortion. To examine the structural evolution with temperature in the present film, temperature-dependent XRD measurements have been taken down to 20 K. The lattice parameter for both film and substrate has been calculated from the Bragg peak. The lattice parameters related to the (100) and (200) peaks of the $SrIrO_3$ film and the (200) peak of the $SrTiO_3$ substrate are shown in Figs. 10(a), 10(b), and 10(c), respectively.

Here, it can be mentioned that the lattice parameters determined from the (100) and (200) peaks of $SrIrO_3$ exhibit a minor difference (∼0.003 Å) at room temperature, which is maybe due to the fact that their 2θ positions are different. Nonetheless, this difference in lattice parameters remains almost similar across the temperature range [Figs. 10(a) and 10(b)]. Figure 10 shows that the lattice parameters of the film and substrate do not follow the same behavior, particularly at low temperatures. Both the $SrIrO_3$ lattice parameters related to the (100) and (200) Bragg peaks initially decrease with decreasing temperature till around 40 K and then show a sudden increase. On the other hand, the lattice parameter of the $SrTiO_3$ substrate shows a continuous decrease indicating an anomaly around 100 K [Fig. 10(c)]. This anomaly arises because $SrTiO_3$ has a structural phase transition from room-temperature cubic to tetragonal phase at 105 K where the lattice parameters show a minor difference at low temperature. However, this structural phase transition of the $SrTiO_3$ substrate will unlikely influence the magnetic ordering of the $SrIrO_3$ film as the former happens at a relatively high temperature. As evident in Fig. 10, the difference between the lattice parameters of the film and substrate increases at low temperature, which generates strain resulting in more distortion in local structure. The IrO_6 octahedra become distorted in terms of Ir–O bond length and bond angle, which will have large ramifications on the magnetic and electronic properties.

IV. SUMMARY AND CONCLUSION

$SrIrO_3$ lies at the boundary of magnetic instability where a close interplay between SOC and U has been shown to give rise to many exotic magnetic and electronic phases in this material [12]. Even realization of topological phases through tuning of SOC in $SrIrO_3$ has been discussed using band structure calculations [14]. The semimetallic electronic structure in $SrIrO_3$, which is characterized by line nodes and small density of states, makes this material quite interesting compared with layered Sr_2IrO_4 and $Sr_3Ir_2O_7$, which are both magnetic and insulating. In this Ruddlesden-Popper-series-based oxide, the corner-shared IrO_6 octahedra play a crucial role in stabilizing its physical properties. An increasing lattice strain realized from the underlying substrate would introduce a structural distortion at low temperatures in terms of modification of the bond angle and bond length between Ir and oxygen. Therefore the IrO_6 octahedra will be distorted with a modified local environment which will influence the three-dimensional network of the Ir-O-Ir chain. Usually, both SOC and U are considered to be intrinsic atomic properties, which would largely remain unaltered in the present case with no change in transition metal or its electronic configuration. The particular combination of SOC and U is not energetically favorable for the onset of magnetic ordering in bulk $SrIrO_3$, even in the presence of magnetic Ir^{4+} ($J_{\text{eff}} = 1/2$). However, the IrO_6 octahedral (structural) distortion with modified bandwidth and electronic structure would compete with these energies. Therefore a strong competition among SOC, U, structural distortion, and bandwidth will eventually weaken the effective strength of SOC and promote the magnetic exchange. These would drive the system into different magnetic and electronic states.

The structural-distortion-driven magnetism has already been evidenced in doped bulk $SrIr_{1-x}Sn_xO_3$, where the substitution of nonmagnetic, isovalent Sn^{4+} for Ir^{4+} induces a metal-to-insulator transition and an antiferromagnetic transition ($T_N \geqslant 225$ K) which has been explained as the combined effect of increased spin-spin exchange interaction, decreased SOC, and enhanced IrO_6 octahedral distortion [15]. Furthermore, a dimensionality-induced magnetic ordering and its relation to a resistivity anomaly have been shown in the $[(SrIrO_3)_m, (SrTiO_3)_n]$ superlattice, where the properties are shown to largely depend on both m and n [26,27]. Very recently, an evolution of magnetic moment as well as electrical properties with structural distortion has been shown in the $3d$-$5d$ double perovskite $(Sr_{1-x}Ca_x)_2FeIrO_6$ using both experimental data and theoretical calculations [45]. A complex orbital ordering with AFM spin state has been shown in another double perovskite, Sr_2CeIrO_6, as a competition between SOC, U, and structural distortion [49]. Here, it can be noted that in our previous $La_{0.67}Sr_{0.33}MnO_3/SrIrO_3$ multilayer, we have observed an interface magnetic exchange interaction and related exchange bias effect below 40 K. Although a different magnetic state (weak FM ordering) is observed in the present film compared with bulk doped $SrIr_{1-x}Sn_xO_3$, an increasing structural distortion at low temperature likely triggers the FM

ordering in the present $SrIrO_3$ film. Nonetheless, iridates in general have a delicate balance among different competing energies such as electron correlation, SOC, and the crystal field effect; therefore tuning of any parameter leads to modification of electric and magnetic properties.

In summary, we have prepared an epitaxial thin film of $SrIrO_3$ (∼40 nm) on $SrTiO_3$ (100) substrate. Structural analysis shows that the film is of good quality. In contrast to bulk material, the film shows an insulating behavior where the charge transport mechanism follows Mott's variable-range-hopping model. Furthermore, magnetic measurements suggest a development of weak FM ordering at low temperature below ∼20 K. The magnetoresistance at 2 K is found to be positive showing a quadratic field dependence in the low-field regime (<40 kOe). A nonlinear Hall effect is observed at low temperature below 20 K which is believed to be caused by an anomalous Hall behavior. The present film further shows an anisotropic magnetoresistance and Hall voltage at low temperatures. These experimental observations are in favor of a FM state at low temperature. A sudden increase in the lattice parameter below ∼40 K implies an increase in lattice strain, which causes (local) structural distortion that is believed to induce the low-temperature FM ordering of the $SrIrO_3$ film. Given that $SrIrO_3$ has a delicate energy balance of SOC, dimensionality, and structural distortion which places this material in close proximity to FM instability and metal-insulator transition, our study shows that lattice strain plays a vital role in tuning the physical properties in this simple, though unusual oxide.

ACKNOWLEDGMENTS

We acknowledge SERB-DST for funding the excimer laser, PURSE-DST for funding the helium liquefier, FIST-DST for funding the low-temperature high-magnetic-field AFM/scanning tunneling microscope (STM), and UPE II-UGC for funding the film deposition chamber. We are thankful to Dr. Alok Banerjee and Dr. Rajeev Rawat, UGC-DAE CSR, Indore, and Dr. Ajay Kumar Shukla, NPL, Delhi, for the magnetization, electrical resistivity, and thin-film XRD measurements and discussions. R.C. is thankful to UGC, India, for financial support.

[1] B. J. Kim, H. Jin, S. J. Moon, J.-Y. Kim, B.-G. Park, C. S. Leem, J. Yu, T. W. Noh, C. Kim, S.-J. Oh, J.-H. Park, V. Durairaj, G. Cao, and E. Rotenberg, Phys. Rev. Lett **101**, 076402 (2008).

[2] B. J. Kim, H. Ohsumi, T. Komesu, S. Sakai, T. Morita, H. Takagi, and T. Arima, Science **323**, 1329 (2009).

[3] W. Witczak-Krempa, G. Chen, Y. B. Kim, and L. Balents, Annu. Rev. Condens. Matter Phys. **5**, 57 (2014).

[4] G. Cao, A. Subedi, S. Calder, J.-Q. Yan, J. Yi, Z. Gai, L. Poudel, D. J. Singh, M. D. Lumsden, A. D. Christianson, B. C. Sales, and D. Mandrus, Phys. Rev. B **87**, 155136 (2013).

[5] P. E. R. Blanchard, E. Reynolds, B. J. Kennedy, J. A. Kimpton, M. Avdeev, and A. A. Belik, Phys. Rev. B **89**, 214106 (2014).

[6] J. M. Longo, J. A. Kafalas, and R. J. Arnott, J. Solid State Chem. **3**, 174 (1971).

[7] S. J. Moon, H. Jin, K. W. Kim, W. S. Choi, Y. S. Lee, J. Yu, G. Cao, A. Sumi, H. Funakubo, C. Bernhard, and T. W. Noh, Phys. Rev. Lett **101**, 226402 (2008).

[8] J. G. Rau, E. K.-H. Lee, and H.-Y. Kee, Annu. Rev. Condens. Matter Phys. **7**, 195 (2016).

[9] I. Pallecchi, M. T. Buscaglia, V. Buscaglia, E. Gilioli, G. Lamura, F. Telesio, M. R. Cimberle, and D. Marré, J. Phys.: Condens. Matter **28**, 065601 (2016).

[10] G. Cao, Y. Xin, C. S. Alexander, J. E. Crow, P. Schlottmann, M. K. Crawford, R. L. Harlow, and W. Marshall, Phys. Rev. B **66**, 214412 (2002).

[11] I. N. Bhatti, R. Rawat, A. Banerjee, and A. K. Pramanik, J. Phys.: Condens. Matter **27**, 016005 (2014).

[12] M. A. Zeb and H.-Y. Kee, Phys. Rev. B **86**, 085149 (2012).

[13] G. Cao, V. Durairaj, S. Chikara, L. E. DeLong, S. Parkin, and P. Schlottmann, Phys. Rev. B **76**, 100402(R) (2007).

[14] J.-M. Carter, V. V. Shankar, M. A. Zeb, and H.-Y. Kee, Phys Rev. B **85**, 115105 (2012).

[15] Q. Cui, J.-G. Chen, W. Fan, A. E. Taylor, S. Calder, M. A. McGuire, J.-Q. Yan, D. Meyers, X. Li, Y. Q. Cai, Y. Y. Jiao, Y. Choi, D. Haskel, H. Gotou, Y. Uwatoko, J. Chakhalian, A. D. Christianson, S. Yunoki, J. B. Goodenough, and J.-S. Zhou, Phys. Rev. Lett. **117**, 176603 (2016).

[16] J. G. Zhao, L. X. Yang, Y. Yu, F. Y. Li, R. C. Yu, Z. Fang, L. C. Chen, and C. Q. Jin, J. Appl. Phys. (Melville, NY) **103**, 103706 (2008).

[17] Y. F. Nie, P. D. C. King, C. H. Kim, M. Uchida, H. I. Wei, B. D. Faeth, J. P. Ruf, J. P. C. Ruff, L. Xie, X. Pan, C. J. Fennie, D. G. Schlom, and K. M. Shen, Phys. Rev. Lett **114**, 016401 (2015).

[18] L. Zhang, Q. Liang, Y. Xiong, B. Zhang, L. Gao, H. Li, Y. B. Chen, J. Zhou, S.-T. Zhang, Z.-B. Gu, S.-H. Yao, Z. Wang, Y. Lin, and Y.-F. Chen, Phys. Rev. B **91**, 035110 (2015).

[19] A. Biswas and Y. H. Jeong, J. Phys. D: Appl. Phys. **48**, 135303 (2015).

[20] A. Biswas, K.-S. Kim, and Y. H. Jeong, J. Appl. Phys. (Melville, NY) **116**, 213704 (2014).

[21] S. G. Bhat, N. Gauquelin, N. K. Sebastian, A. Sil, A. Béché, J. Verbeeck, D. Samal, and P. S. Anil Kumar, EPL **122**, 28003 (2018).

[22] J. Matsuno, N. Ogawa, K. Yasuda, F. Kagawa, W. Koshibae, N. Nagaosa, Y. Tokura, and M. Kawasaki, Sci. Adv. **2**, e1600304 (2016).

[23] J. Nichols, X. Gao, S. Lee, T. L. Meyer, J. W. Freeland, V. Lauter, D. Yi, J. Liu, D. Haskel, J. R. Petrie, E.-J. Guo, A. Herklotz, D. Lee, T. Z. Ward, G. Eres, M. R. Fitzsimmons, and H. N. Lee, Nat. Commun. **7**, 12721 (2016).

[24] R. Chaurasia, K. C. Kharkwal, and A. K. Pramanik, Phys. Lett. A **383**, 1642 (2019).

[25] D. Yi, J. Liu, S.-L. Hsu, L. Zhang, Y. Choi, J.-W. Kim, Z. Chen, J. D. Clarkson, C. R. Serrao, E. Arenholz, P. J. Ryan, H. Xu, R. J. Birgeneau, and R. Ramesh, Proc. Natl. Acad. Sci. USA **113**, 6397 (2016).

[26] J. Matsuno, K. Ihara, S. Yamamura, H. Wadati, K. Ishii, V. V. Shankar, H.-Y. Kee, and H. Takagi, Phys. Rev. Lett. **114**, 247209 (2015).

[27] L. Hao, D. Meyers, C. Frederick, G. Fabbris, J. Yang, N. Traynor, L. Horak, D. Kriegner, Y. Choi, J.-W. Kim, D. Haskel, P. J. Ryan, M. P. M. Dean, and J. Liu, Phys. Rev. Lett. **119**, 027204 (2017).

[28] S. Tripathi, R. Rana, S. Kumar, P. Pandey, R. S. Singh, and D. S. Rana, Sci. Rep. **4**, 3877 (2014).

[29] K. C. Kharkwal, R. Chaurasia, and A. K. Pramanik, J. Phys.: Condens. Matter **31**, 13LT02 (2019).

[30] L. Zhang, B. Pang, Y. B. Chen, and Y. Chen, Crit. Rev. Solid State Mater. Sci. **43**, 367 (2018).

[31] S. Y. Jang, S. J. Moon, B. C. Jeon, and J. S. Chung, J. Korean Phys. Soc. **56**, 1814 (2010).

[32] M. A. Laguna-Marco, P. Kayser, J. A. Alonso, M. J. Martínez-Lope, M. van Veenendaal, Y. Choi, and D. Haskel, Phys. Rev. B **91**, 214433 (2015).

[33] G. Zhou, X. Gu, X. Yang, X. Gao, K. Wang, J. Peng, F. Zhang, and X. S. Wu, AIP Adv. **7**, 055823 (2017).

[34] X. Liu, Y. Cao, B. Pal, S. Middey, M. Kareev, Y. Choi, P. Shafer, D. Haskel, E. Arenholz, and J. Chakhalian, Phys. Rev. Mater. **1**, 075004 (2017).

[35] H. Kumar, K. C. Kharkwal, K. Kumar, K. Asokan, A. Banerjee, and A. K. Pramanik, Phys. Rev. B **101**, 064405 (2020).

[36] J. P. Clancy, N. Chen, C. Y. Kim, W. F. Chen, K. W. Plumb, B. C. Jeon, T. W. Noh, and Y.-J. Kim, Phys. Rev. B **86**, 195131 (2012).

[37] K. C. Kharkwal, R. K. Patel, K. Asokan, and A. K. Pramanik, J. Phys.: Condens. Matter **32**, 505001 (2020).

[38] G. L. Stamokostas and G. A. Fiete, Phys. Rev. B **97**, 085150 (2018).

[39] I. Qasim, B. J. Kennedy, and M. Avdeev, J. Mater. Chem. A **1**, 13357 (2013).

[40] J. Nogués and I. K. Schuller, J. Magn. Magn. Mater. **192**, 203 (1999).

[41] X. Ke, M. S. Rzchowski, L. J. Belenky, and C. B. Eom, Appl. Phys. Lett. **84**, 5458 (2004).

[42] H. Y. Hwang, Y. Iwasa, M. Kawasaki, B. Keimer, N. Nagaosa, and Y. Tokura, Nat. Mater. **11**, 103 (2012).

[43] P. Zubko, S. Gariglio, M. Gabay, P. Ghosez, and J.-M. Triscone, Annu. Rev. Condens. Matter Phys. **2**, 141 (2011).

[44] C. Sow, A. K. Pramanik, and P. S. Anil Kumar, J. Appl. Phys. (Melville, NY) **116**, 194310 (2014).

[45] K. C. Kharkwal, R. Roy, H. Kumar, A. K. Bera, S. M. Yusuf, A. K. Shukla, K. Kumar, S. Kanungo, and A. K. Pramanik, Phys. Rev. B **102**, 174401 (2020).

[46] N. Mott, *Conduction in Non-crystalline Materials* (Clarendon, Oxford, 1993).

[47] F.-X. Wu, J. Zhou, L. Y. Zhang, Y. B. Chen, S.-T. Zhang, Z.-B. Gu, S.-H. Yao, and Y.-F. Chen, J. Phys.: Condens. Matter **25**, 125604 (2013).

[48] N. Nagaosa, J. Sinova, S. Onoda, A. H. MacDonald, and N. P. Ong, Rev. Mod. Phys. **82**, 1539 (2010).

[49] S. Kanungo, K. Mogare, B. Yan, M. Reehuis, A. Hoser, C. Felser, and M. Jansen, Phys. Rev. B **93**, 245148 (2016).